Superconductivity in undoped $BaFe_2As_2$ by tetrahedral geometry design

Jong-Hoon Kang[a], Jong-Woo Kim[b], Philip J. Ryan[b,c], Lin Xie[d], Lu Guo[a], Chris Sundahl[a], Jonathon Schad[a], Neil Campbell[e], Yesusa G. Collantes[f], Eric E. Hellstrom[f], Mark S. Rzchowski[e], and Chang-Beom Eom[a,1]

[a]Department of Materials Science and Engineering, University of Wisconsin–Madison, Madison, WI 53706; [b]Advanced Photon Source, Argonne National Laboratory, Argonne, IL 60439; [c]School of Physical Sciences, Dublin City University, Dublin 9, Ireland; [d]Department of Physics, Southern University of Science and Technology, 518055 Shenzhen, China; [e]Department of Physics, University of Wisconsin–Madison, Madison, WI 53706; and [f]Applied Superconductivity Center, National High Magnetic Field Laboratory, Florida State University, Tallahassee, FL 32310

Edited by Zachary Fisk, University of California, Irvine, CA, and approved July 17, 2020 (received for review January 19, 2020)

Fe-based superconductors exhibit a diverse interplay between charge, orbital, and magnetic ordering. Variations in atomic geometry affect electron hopping between Fe atoms and the Fermi surface topology, influencing magnetic frustration and the pairing strength through changes of orbital overlap and occupancies. Here, we experimentally demonstrate a systematic approach to realize superconductivity without chemical doping in $BaFe_2As_2$, employing geometric design within an epitaxial heterostructure. We control both tetragonality and orthorhombicity in $BaFe_2As_2$ through superlattice engineering, which we experimentally find to induce superconductivity when the As–Fe–As bond angle approaches that in a regular tetrahedron. This approach to superlattice design could lead to insights into low-dimensional superconductivity in Fe-based superconductors.

superconductivity | atomic geometry | epitaxial heterostructure | low-dimension | superlattice

Atomic arrangement of complex materials can be fine-tuned in epitaxial thin films and heterostructures and subsequently enhance the superconducting transition temperature (T_c), as recently demonstrated in single-layer FeSe (1, 2). More complex high-T_c superconductors such as Co-doped $BaFe_2As_2$ have technical challenges such as structural and chemical disorder at surfaces and interfaces, but also offer the promise of inducing and enhancing superconductivity with structural control. Highly ordered and controlled interfaces can host superconducting properties superior to that of bulk materials (3–11). Here, we present the atomic engineering to control and measure interfacial driven superconductivity in Fe-based compounds. The atomically sharp interfaces in undoped $BaFe_2As_2$ (Ba-122)/$SrTiO_3$ (STO) superlattice systems offer advancement in the precise control of atomic structures.

The relation between atomic structure and electronic properties of superconducting $Ba(Fe_{1-x}Co_x)_2As_2$ and the parent compound $BaFe_2As_2$ has emerged as the key to understanding the complex nature of these materials, including the low-temperature superconducting state. The nematic phase arising at the structural transition temperature (T_s) breaks the 90° rotation symmetry of the high-temperature phase, necessarily exhibiting structural, orbital, and spin-driven nematic order (12–24), with antiferromagnetic order setting in at magnetic phase transition temperature (T_n) lower than T_s. Increased Co doping pushes the magnetic transition farther below the structural orthorhombic (nematic) transition, and suppresses both associated order parameters. This correlates with the emergence of the low-temperature superconducting phase, which competes with static magnetic order. The highest superconducting transition temperature T_c is obtained at the Co doping for which not only is the orthorhombicity smallest but also the Fe–As bonds form a symmetric tetrahedral arrangement.

An important question is the driving force behind these effects, whether spin, charge, or structural order parameter plays an important role. Substitutional doping affects electronic interactions, which, in turn, influence other orders in the material. Here we demonstrate the separate importance of orthorhombicity and tetrahedral coordination by inducing superconductivity in the undoped parent compound $BaFe_2As_2$ by strain and symmetry control. We accomplish this by alternating ultrathin layers of $BaFe_2As_2$ with $SrTiO_3$ in an epitaxial superlattice grown on a CaF_2 substrate. The substrate provides initial biaxial strain, and the $SrTiO_3$ layers maintain that strain throughout the superlattice. The square template of both of these layers suppresses the orthorhombicity of low-temperature $BaFe_2As_2$, with the thinnest $BaFe_2As_2$ layers remaining almost fully tetragonal to low temperature. The undoped superlattice becomes superconducting, and the transition temperature increases with decreasing $BaFe_2As_2$ orthorhombicity, and with decreasing differences between Fe–As bond angles. We argue that structural control is an important contributor to superconductivity in Fe-based superconductors.

In parent Ba-122 bulk single crystals (Fig. 1*A*), the Fe sublattice undergoes a symmetry-breaking magnetostructural phase transition at low temperature, distorting the $FeAs_4$ tetrahedron and altering all bond angles α, β, and γ, and changing the overall symmetry from tetragonal to orthorhombic. The magnetic ordering in the quasi–two-dimensional layer of the distorted $FeAs_4$ tetrahedra is believed to suppress superconductivity in bulk Ba-122 materials (25, 26). However, we demonstrate superconductivity by tuning the system toward a higher-symmetry structure, namely, a regular tetrahedral arrangement (27) in high-quality epitaxial Ba-122/STO superlattice films on (001) CaF_2 substrates (*Materials and Methods* and *SI Appendix*, section 1). This is achieved via the manipulation of in-plane symmetry (orthorhombicity at low temperature) and the ratio between out-of-plane and in-plane

Significance

The results demonstrated here show superconductivity in the antiferromagnetic $BaFe_2As_2$ without chemical substitution, by atomic level control of local structure through epitaxial superlattice design. The interfacial interactions modify the $FeAs_4$ tetrahedra via systematic control of tetragonal and orthorhombic structures, inducing superconductivity. This indicates structure and dimensionality play an important role in the superconducting properties in Fe-based superconductors, and opens a path to structural manipulation of superconductivity in ultrathin layers of Fe-based materials. This is likely to play a major role in understanding and developing Fe-based superconductors.

Author contributions: J.-H.K., M.S.R., and C.-B.E. designed research; J.-H.K., J.-W.K., P.J.R., L.X., L.G., C.S., J.S., N.C., and Y.G.C. performed research; J.-H.K., J.-W.K., P.J.R., L.X., N.C., and M.S.R. analyzed data; J.-H.K., E.E.H., M.S.R., and C.-B.E. wrote the paper; E.E.H. supervised research; and C.-B.E. directed the research.

The authors declare no competing interest.

This article is a PNAS Direct Submission.

[1]To whom correspondence may be addressed. Email: ceom@wisc.edu.

This article contains supporting information online at https://www.pnas.org/lookup/suppl/doi:10.1073/pnas.2001123117/-/DCSupplemental.

First published August 17, 2020.

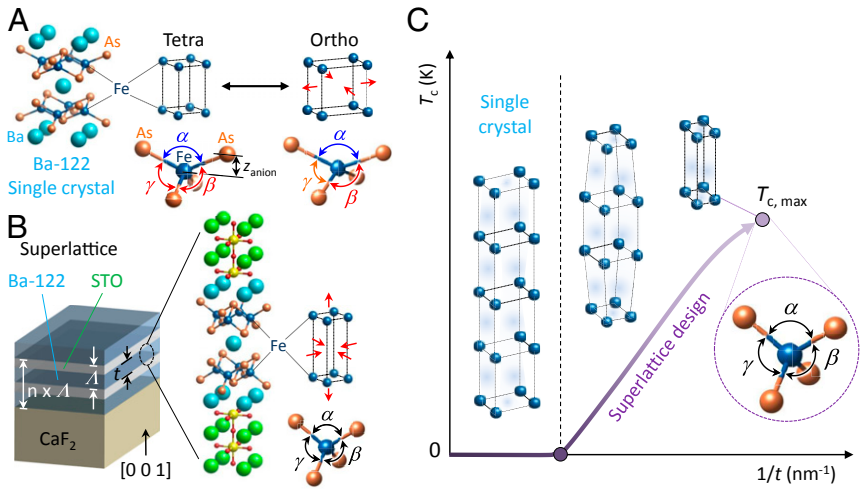

Fig. 1. Emergent superconductivity in parent Ba-122 by superlattice design. (*A*) Fe sublattice and tetrahedral geometry in Ba-122 bulk single crystal below magnetostructural phase transition temperature. (*B*) Superlattice design for the control of Fe sublattice structure and $FeAs_4$ tetrahedron in the presence of tetragonal-to-orthorhombic transition. (*C*) Emergent superconductivity by proximity to the regular tetrahedron via reduction of the Ba-122 layer thickness *t* in a Ba-122/$SrTiO_3$ superlattice.

lattice parameter (tetragonality at high temperature) of the Fe sublattice structures (Fig. 1*B*).

The superlattice system provides a mechanism to control the $FeAs_4$ tetrahedron of the Ba-122 layers for emergent superconductivity. First, bulk Ba-122 has anisotropic in-plane lattice constants associated with the tetragonal-to-orthorhombic transition, causing the β and γ bond angles to differ. We found that the orthorhombic transition is suppressed by in-plane clamping arising from epitaxy with STO, leading to equal β and γ. Secondly, tetragonal Ba-122 without the orthorhombic distortion still has a bond angle difference between α and β, as they are set by the in-plane lattice and the anion (Arsenic) *z* height (22, 28) (*Materials and Methods* and *SI Appendix*, section 2). Since, in bulk Ba-122, α is larger than β as shown in Fig. 1*A*, reducing the in-plane lattice and expanding the anion *z* height drives the bond angle α toward β, through biaxial compressive strain imposed by CaF_2 substrates. The regular tetrahedron can be achieved by tetragonal elongation where all bond angles approach 109.5° (Fig. 1*B*).

The reduction of Ba-122 thickness (*t*) in the superlattice structure decreases degree of orthorhombic distortion and increases *c* elongation of tetragonal structure because the rigidity from STO transmits the compressive strain and the square symmetry more effectively through throughout the Ba-122 film (Fig. 1*C*). However, the clamping effect on both the top and bottom of the Ba-122 layer is insufficient to fully suppress the orthorhombic transition. The superlattice Ba-122 layers experience a strain gradient (showing a broad superconducting transition), but the average values of structural and electrical properties tuned by the thickness of Ba-122 layer clearly demonstrate the influence of tetrahedral geometry on T_c.

We performed atomic resolution scanning transmission electron microscopy (STEM) combined with energy-dispersive X-ray spectroscopy (EDX) to investigate the microstructure, chemistry, and interfacial structure of the superlattice system (Fig. 2). Fig. 2*A* shows a cross-sectional high-angle annular dark field (HAADF) image of the 12-layer Ba-122/STO superlattice structure with a total thickness of 260 nm (see *Materials and Methods*). Bright

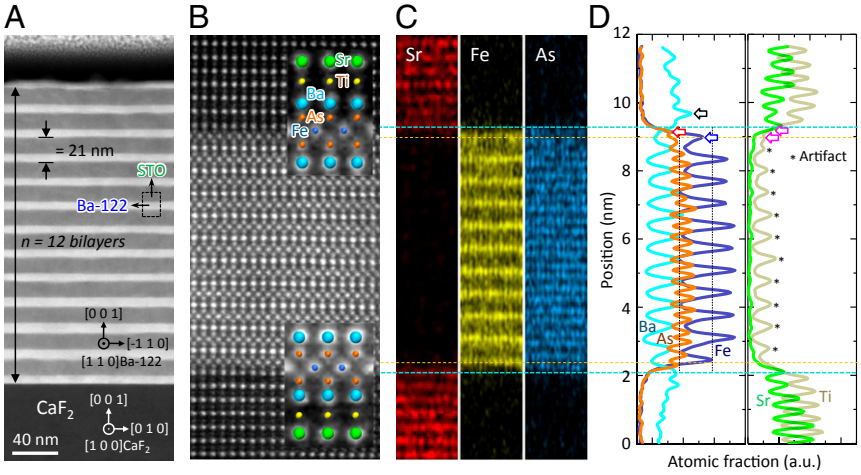

Fig. 2. Microstructure and atomic arrangement in Ba-122/STO superlattice thin films. (*A*) HAADF image of 12 layers of $Ba\text{-}122_{7nm}/STO_{14nm}$ superlattice on CaF_2 substrate. (*B*) High-resolution HAADF image of <1 1 0> projection of the Ba-122/STO heterointerfaces. Insets are enlarged images of interfacial structures. (*C*) EDX line scan across an STO insertion layer, a Ba-122 layer, and the interface of a Ba-122/STO. (*D*) Atomic fraction extracted from the EDX line scan showing the layered distribution of each element.

and dark layers in the image correspond to 7-nm-thick Ba-122 and 14-nm-thick STO layers, respectively. The thickness of each layer and the modulation wavelength (Λ) are in accordance with the structural information determined by satellite peaks in synchrotron X-ray diffraction (XRD) patterns (*SI Appendix*, section 3). Fig. 2*B* shows a high-resolution HAADF image of the interfacial region of the STO/Ba-122/STO structure (black dashed box in Fig. 2*A*). Individual atoms of the Ba-122, STO, and interfaces are distinguishable (Fig. 2 *B*, *Insets*). The Ba-122/STO heterostructure has atomically sharp interfaces at both the top and bottom regions.

Interfacial imperfections such as chemical intermixing between Ba-122 and STO are investigated with EDX. The elemental mapping by EDX shows there is no severe chemical reaction, diffusion, or intermixing between Ba-122 and STO layers, and we can clearly see the layered distribution of Sr and Fe/As atoms in STO and Ba-122, respectively (Fig. 2*C*). The EDX line scan indicates that the bottom interface of the Ba-122 layer has less interdiffusion/intermixing than the top (Fig. 2*D*). Previous theoretical calculations on the STO/Ba-122 interface support suppressed intermixing at the bottom interface, as the Ba layer is thermodynamically stable on TiO_2-terminated STO with an atomically sharp interface (29). In contrast, there are a small number of As and Fe atoms missing in Ba-122 underneath the top interface (red and blue arrows) due to Ti diffusion (purple arrows). Ba diffusion into the STO is also found above the interface (black arrows). The EDX scan indicates that a Ba/Sr interfacial layer on the As layer (30, 31) is unstable during the STO growth, allowing a small degree of intermixing at the interface. Since Ti-K_α edge is overlapped with Ba-L_α in EDX (indicated by an asterisk in Fig. 2*D*), we confirm that there are no Ti and O atoms in the Ba-122 layer with electron energy loss spectroscopy (*SI Appendix*, section 4).

The detailed structure of superlattice Ba-122 was investigated by synchrotron XRD in Fig. 3 (*Materials and Methods* and *SI Appendix*, section 5). We measured the Ba-122 (2 2 8) reflections to examine the tetragonal-to-orthorhombic transition (32) as a function of temperature. As temperature decreases, the peak broadens due to the orthorhombic distortion below the phase transition temperature (*SI Appendix*, section 5). The reflection was fitted with two peaks using the full width at half maximum (FWHM) of the tetragonal phase taken at room temperature represented by the purple and dark blue curves in Fig. 3*A*. The orthorhombic distortion is clearly shown in the thicker Ba-122, whereas it is reduced in the 3.5-nm-thick Ba-122 layers. From the fitted peak positions of (2 2 8) and (0 0 L) reflections, we calculate orthorhombic *a*, *b*, and *c* lattice parameters. The temperature-dependent in-plane lattice parameters are shown for different Ba-122 thicknesses in Fig. 3*B*. The $SrTiO_3$ layer thickness is kept constant at 14 nm, and all superlattices consist of 12 bilayers. Higher compressive biaxial strain and the larger *c* axis elongation are observed in the thinner Ba-122 layers. As the Ba-122 is grown thinner, the structural transition temperature (T_s) shifts lower (indicated by arrows), and the difference between in-plane lattice parameters becomes smaller.

We performed anomalous X-ray scattering at the As-*K* edge to extract the precise local structure of the $FeAs_4$ tetrahedron. The extent of intensity variation in energy scans of the (0 0 L) at the absorption edges reflects the amount of As scattering contribution to the diffraction intensity, which is directly coupled to the *z* position (*Materials and Methods* and *SI Appendix*, section 5). Combining the lattice parameters with the As relative *z* position, the complete $FeAs_4$ configuration is obtained. Fig. 3*C* demonstrates that the As–Fe–As bond angles are controlled by the Ba-122 thickness. The three bond angles α, β, and γ in the tetrahedron are all different in thicker Ba-122 layers, due to the orthorhombic symmetry. As the Ba-122 thickness decreases, the difference between the bond angles reduces until finally there is a negligible difference at 3.5 nm, showing an ideal tetrahedron bond angle (23, 27) of 109.5°. The ideal tetrahedron is obtained via both the suppression of orthorhombicity by the clamping effect and the manipulation of the tetragonal structure by the compressive biaxial strain. Therefore, the superlattice design with the Ba-122 thickness control makes it possible to realize the regular tetrahedron in parent Ba-122 (*SI Appendix*, section 5).

To investigate the influence of tetrahedral geometry on superconducting T_c, temperature-dependent resistivity (Fig. 4*A*) was measured in a van der Pauw geometry. The data show resistive anomalies corresponding to the structural and magnetic transitions. We assigned the structural phase transition temperature (T_s) to the onset of the first derivative of the resistivity, and the magnetic phase transition temperature (T_n) to the maximum in the first derivative of the resistivity with respect to temperature (26, 32, 33) (*SI Appendix*, section 6). Reduction of T_s with decreasing the Ba-122 thickness is consistent with the suppression of the orthorhombic distortion characterized by X-ray measurements as shown in Fig. 3*B*. Interestingly, T_n also moves to lower temperatures as the structural distortion is suppressed, in agreement with previous reports of antiferromagnetic ordering suppression in parent Ba-122 materials (34, 35). By suppressing the antiferromagnetically ordered orthorhombic phase, we observed emergent superconductivity and increased T_c up to 9 K in the superlattice sample with thinner Ba-122 layers (Fig. 4 *A*, *Inset*). It is clearly shown that the T_c increases from 0 K to 9 K as the

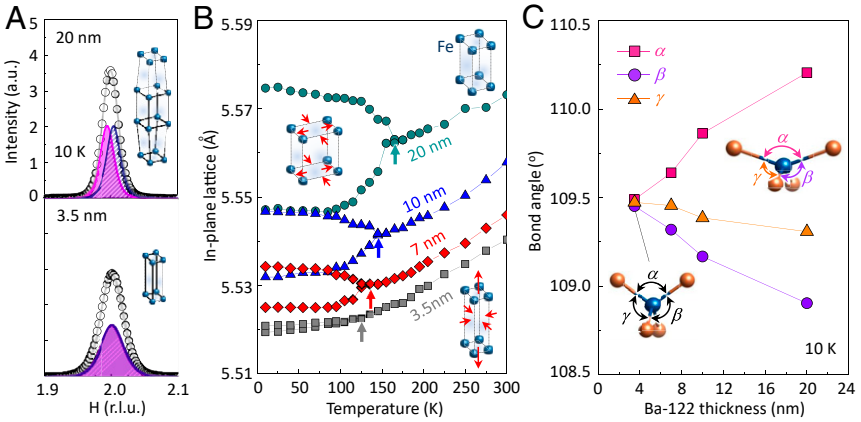

Fig. 3. Atomic structure of Ba-122 in the superlattice investigated by synchrotron XRD. (*A*) Tetragonal-to-orthorhombic structural change in (2 2 8) reflection by XRD. (*B*) In-plane lattice parameters as a function of temperature. (*C*) $FeAs_4$ bond angles tuned by Ba-122 thickness. Insets are Fe sublattice and tetrahedral geometry.

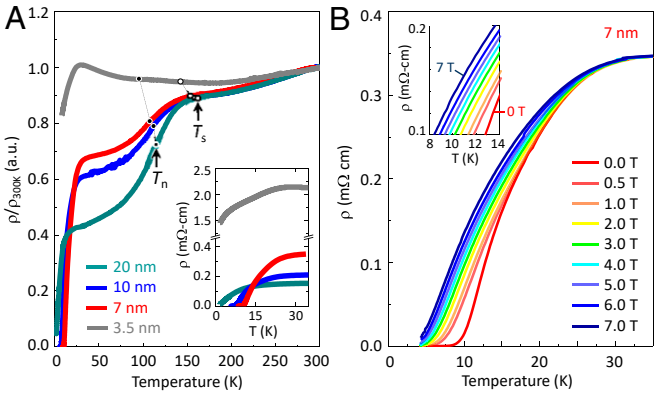

Fig. 4. Superconducting properties of Ba-122/STO superlattice. (*A*) Temperature-dependent resistivity with different Ba-122 thickness. T_s and T_n are structural phase transition and the magnetic phase transition temperature, respectively. (*B*) Superconducting resistive transition with different magnetic field perpendicular to sample surface. Insets are temperature-dependent resistivity near Tc.

Ba-122 thickness decreases from 20 nm to 7 nm. The 3.5-nm-layer-thickness superlattice did not reach zero resistance above 2 K, likely due to localization of Cooper pairs or scattering from the interface (36–38) (*SI Appendix*, section 7).

Fig. 4*B* shows the temperature-dependent resistivity of $Ba\text{-}122_{7nm}/STO_{14nm}$ superlattice in various magnetic field strengths perpendicular to the film surface. It shows a resistive broadening and a lowering of the superconducting transition with increasing magnetic field. However, the current–voltage characteristics in all of the superlattice samples were nonlinear, even under high magnetic fields (*SI Appendix*, section 7), indicating that vortices are strongly pinned in the Ba-122 layer (Fig. 4 *B*, *Inset*), different from weak pinning in other low-dimensional superconductors (39). A zero-field-cooled magnetization T_c was measured to show clear diamagnetic signal by superconducting quantum interference device magnetometer measurements (*SI Appendix*, section 7). The chemical homogeneity of the undoped $BaFe_2As_2$ layers, and the uniformity of structural changes controlled by the $SrTiO_3$ layers, make nonuniform phenomena such as filamentary superconductivity unlikely.

Fig. 5 shows the temperature–thickness phase diagram of the parent Ba-122 in the superlattice system obtained from our experimental data. Structural (T_s) and magnetic (T_n) phase transition temperatures and superconducting critical temperature (T_c) are shown. Note that T_s was extracted from the bifurcation point of the in-plane lattice constants measured by synchrotron XRD, and T_n was extracted from the maximum in the first derivative of the resistivity with respect to temperature (*SI Appendix*, section 6). The structural transition does not exhibit a first-order phase transition that is found in Ba-122 single crystals (26, 32, 33), and T_n deviates considerably from T_s, similar to the effects of electron doping. As the Ba-122 thickness decreases to lower dimensions, both T_s and T_n decrease, indicating a suppression of both nematic and magnetic ordering due to biaxial strain. While T_s and T_n decrease, T_c increases because the broken symmetry phase, which maintains magnetic ordering and competes with superconductivity, diminishes.

The atomic engineering demonstrated here enables precise control of the $FeAs_4$ tetrahedral geometry, and provides a platform to understand the connection between local structure and superconductivity. Reduction of the Ba-122 layer thickness manipulates the tetrahedra via systematic control of tetragonal and orthorhombic structures, and results in an enhanced superconducting T_c. We believe that the superlattice approach provides a pathway to overcome the limited ability to T_c control in the ultrathin films of the Fe-based superconductors (2, 40). Furthermore, this study will open up opportunities to study low-dimensional superconductivity and to explore phenomena in Fe-based superconductors.

Materials and Methods

Epitaxial Growth. Epitaxial Ba-122/STO superlattices (*SI Appendix*, sections 1 and 3) were grown on (001) CaF_2 single-crystal substrates by pulsed laser deposition with a KrF (248 nm) ultraviolet excimer laser at 740 °C. The base pressure before the deposition was 3×10^{-5} Pa, and the deposition took place at 3×10^{-4} Pa because of the degassing of the heater. Temperature-dependent in-plane lattice change of the Ba-122 is driven by the thermal expansion coefficient (CTE) of CaF_2 substrate (*SI Appendix*, section 5). We found that fluoride substrates with higher CTE are more effective to provide compressive biaxial strain, rather than oxide substrates. Note that the CTE of CaF_2 is 1.9×10^{-5}/K at 300 K, higher than that of Ba-122 with 1.0×10^{-6}/K.

STEM HAADF and EDX Experiments. Atomic-resolution STEM HAADF experiments were carried out on a double aberration-corrector transmission electron microscope, which was operated at 300 kV and has a resolution of ~0.6 Å. A series of STEM HAADF images were obtained at a resolution of 1,024 × 1,024 pixels, with a dwell time for each pixel of ~0.5 μs. Then the acquired images were summed by removing the drift between each image using the cross-correlation method. EDX spectra were acquired by Super-X detectors and processed in software Velox.

Synchrotron X-Ray Techniques. High-resolution XRD and resonant X-ray scattering were carried out at beamline 6-ID-B of the Advanced Photon Source (APS) at Argonne National Laboratory. Although the film might have

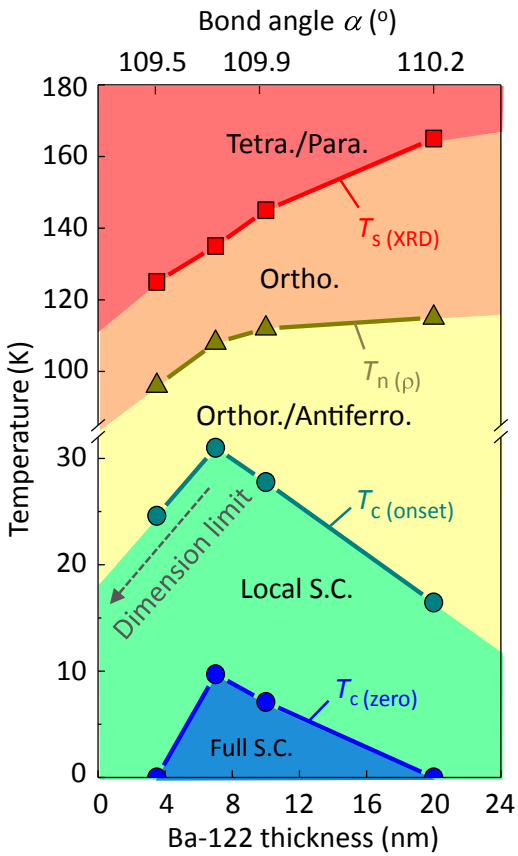

Fig. 5. Temperature versus dimensionality phase diagram of Ba-122 in the superlattice system. Broken symmetry phases are suppressed by controlling the thickness of Ba-122 layer. Superconductivity is initially enhanced in thinner Ba-122 layers, but it is weakened again when the layers get even thinner, possibly as the effect of reduced dimensionality. Tetra., tetragonal; Orthor., orthorhombic; Para., paramagnetic; Antiferro., antiferromagnetic; S.C., superconductivity.

PHYSICS

a small strain gradient along the vertical direction, the XRD measures an average value of lattice parameters. Orthorhombicity is examined by the reciprocal space scan across the (2 2 8) peak. The peak splitting associated with the orthorhombic transition was determined by two-peaks fitting with a fixed reference FWHM obtained from the peak width in the tetragonal phase at room temperature, in order to take into account the natural broadening effect due to the variations in the thickness of Ba-122 layer. Anomalous X-rays scattering as As-*K* edge was performed to measure the relative As position in the unit cell. In symmetry group I4/mmm, only As atom is at the Wyckoff position 4e which takes unspecified *z* position in the unit cell. For the bulk crystal case under hydrostatic pressure, only As relative *z* position varies in published diffraction data. Since the As contribution on diffraction intensity of (0 0 L) Bragg reflection changes by relative *z* position, deriving As portion of diffraction intensity using anomalous X-ray scattering can simply determine the As position.

Data Availability. All data, materials, and associated methods that support the findings of this study are shown in *Materials and Methods* and *SI Appendix*.

ACKNOWLEDGMENTS. This work was supported by the US Department of Energy (DOE), Office of Science, Office of Basic Energy Sciences, under Award DE-FG02-06ER46327. This research used resources of the APS, a US DOE Office of Science User Facility operated for the DOE Office of Science by Argonne National Laboratory under Contract DE-AC02-06CH11357. A portion of the work was done at the National High Magnetic Field Laboratory, which is supported by Program NSF-DMR-1644779 and by the state of Florida. We thank P. J. Hirschfeld, R. Valenti, I. I. Mazin, V. Borisov, and Ian Fisher for helpful discussion.

1. S. He *et al*., Phase diagram and electronic indication of high-temperature superconductivity at 65 K in single-layer FeSe films. *Nat. Mater.* **12**, 605–610 (2013).
2. S. Tan *et al*., Interface-induced superconductivity and strain-dependent spin density waves in FeSe/$SrTiO_3$ thin films. *Nat. Mater.* **12**, 634–640 (2013).
3. A. Gozar *et al*., High-temperature interface superconductivity between metallic and insulating copper oxides. *Nature* **455**, 782–785 (2008).
4. K. Takada *et al*., Superconductivity in two-dimensional CoO_2 layers. *Nature* **422**, 53–55 (2003).
5. H. Shishido *et al*., Tuning the dimensionality of the heavy fermion compound CeIn3. *Science* **327**, 980–983 (2010).
6. N. Reyren *et al*., Superconducting interfaces between insulating oxides. *Science* **317**, 1196–1199 (2007).
7. J. T. Ye *et al*., Liquid-gated interface superconductivity on an atomically flat film. *Nat. Mater.* **9**, 125–128 (2010).
8. J. Chakhalian, A. J. Millis, J. Rondinelli, Whither the oxide interface. *Nat. Mater.* **11**, 92–94 (2012).
9. J. J. Lee *et al*., Interfacial mode coupling as the origin of the enhancement of T_c in FeSe films on $SrTiO_3$. *Nature* **515**, 245–248 (2014).
10. H. Hiramatsu, T. Katase, T. Kamiya, M. Hirano, H. Hosono, Water-induced superconductivity in $SrFe_2As_2$. *Phys. Rev. B Condens. Matter Mater. Phys.* **80**, 052501 (2009).
11. J. Engelmann *et al*., Strain induced superconductivity in the parent compound $BaFe_2As_2$. *Nat. Commun.* **4**, 2877 (2013).
12. Y. Kamihara, T. Watanabe, M. Hirano, H. Hosono, Iron-based layered superconductor $La[O_{1-x}F_x]FeAs$ ($x = 0.05$-0.12) with $T_c = 26$ K. *J. Am. Chem. Soc.* **130**, 3296–3297 (2008).
13. H. Takahashi *et al*., Superconductivity at 43 K in an iron-based layered compound $LaO_{1-x}F_xFeAs$. *Nature* **453**, 376–378 (2008).
14. D. N. Basov, A. V. Chubukov, Manifesto for a higher T_c. *Nat. Phys.* **7**, 272–276 (2011).
15. I. I. Mazin, Superconductivity gets an iron boost. *Nature* **464**, 183–186 (2010).
16. R. M. Fernandes, A. V. Chubukov, J. Schmalian, What drives nematic order in iron-based superconductors? *Nat. Phys.* **10**, 97–104 (2014).
17. Z. P. Yin, K. Haule, G. Kotliar, Kinetic frustration and the nature of the magnetic and paramagnetic states in iron pnictides and iron chalcogenides. *Nat. Mater.* **10**, 932–935 (2011).
18. C. F. Hirjibehedin, Magnetic atoms: The makings of a Hund's metal. *Nat. Nanotechnol.* **10**, 914–915 (2015).
19. H. Hosono, A. Yamamoto, H. Hiramatsu, Y. Ma, Recent advances in iron-based superconductors toward applications. *Mater. Today* **21**, 278–302 (2018).
20. J. Paglione, R. L. Greene, High-temperature superconductivity in iron-based materials. *Nat. Phys.* **6**, 645–658 (2010).
21. C. de la Cruz *et al*., Magnetic order close to superconductivity in the iron-based layered $LaO_{1-x}F_xFeAs$ systems. *Nature* **453**, 899–902 (2008).
22. Y. Mizuguchi *et al*., Anion height dependence of T_c for the Fe-based superconductor. *Supercond. Sci. Technol.* **23**, 054013 (2010).
23. C. H. Lee *et al*., Effect of structural parameters on superconductivity in fluorine-free $LnFeAsO_{1-y}$ (Ln = La, Nd). *J. Phys. Soc. Jpn.* **77**, 8–11 (2008).
24. K. Kuroki *et al*., Pnictogen height as a possible switch between high-T_c nodeless and low-T_c nodal pairings in the iron-based superconductors. *Phys. Rev. B Condens. Matter Mater. Phys.* **79**, 224511 (2009).
25. F. Wang, D. H. Lee, The electron-pairing mechanism of iron-based superconductors. *Science* **332**, 200–204 (2011).
26. M. Rotter *et al*., Spin-density-wave anomaly at 140 K in the ternary iron arsenide $BaFe_2As_2$. *Phys. Rev. B Condens. Matter Mater. Phys.* **78**, 020503 (2008).
27. S. A. Kimber *et al*., Similarities between structural distortions under pressure and chemical doping in superconducting $BaFe_2As_2$. *Nat. Mater.* **8**, 471–475 (2009).
28. H. Okabe, N. Takeshita, K. Horigane, T. Muranaka, J. Akimitsu, Pressure-induced high-T_c superconducting phase in FeSe: Correlation between anion height and T_c. *Phys. Rev. B Condens. Matter Mater. Phys.* **81**, 205119 (2010).
29. J. H. Kang *et al*., Control of epitaxial $BaFe_2As_2$ atomic configurations with substrate surface terminations. *Nano Lett.* **18**, 6347–6352 (2018).
30. F. Massee *et al*., Cleavage surfaces of the $BaFe_{2-x}Co_xAs_2$ and $Fe_ySe_{1-x}Te_x$ superconductors: A combined STM plus LEED study. *Phys. Rev. B Condens. Matter Mater. Phys.* **80**, 140507 (2009).
31. V. B. Nascimento *et al*., Surface geometric and electronic structures of $BaFe_2As_2$(001). *Phys. Rev. Lett.* **103**, 076104 (2009).
32. C. R. Rotundu *et al*., Heat capacity study of $BaFe_2As_2$: Effects of annealing. *Phys. Rev. B Condens. Matter Mater. Phys.* **82**, 144525 (2010).
33. A. Mani, N. Ghosh, S. Paulraj, A. Bharathi, C. S. Sundar, Pressure-induced superconductivity in $BaFe_2As_2$ single crystal. *EuroPhys. Lett.* **87**, 17004 (2009).
34. J. H. Chu *et al*., In-plane resistivity anisotropy in an underdoped iron arsenide superconductor. *Science* **329**, 824–826 (2010).
35. J. H. Chu, H. H. Kuo, J. G. Analytis, I. R. Fisher, Divergent nematic susceptibility in an iron arsenide superconductor. *Science* **337**, 710–712 (2012).
36. M. M. Özer, Y. Jia, Z. Zhang, J. R. Thompson, H. H. Weitering, Tuning the quantum stability and superconductivity of ultrathin metal alloys. *Science* **316**, 1594–1597 (2007).
37. Y. Guo *et al*., Superconductivity modulated by quantum size effects. *Science* **306**, 1915–1917 (2004).
38. S. Qin, J. Kim, Q. Niu, C. K. Shih, Superconductivity at the two-dimensional limit. *Science* **324**, 1314–1317 (2009).
39. Y. Saito, T. Nojima, Y. Iwasa, Highly crystalline 2D superconductors. *Nat. Rev. Mater.* **2**, 16094 (2016).
40. I. Bozovic, C. Ahn, A new frontier for superconductivity. *Nat. Phys.* **10**, 892–895 (2014).